Exploring charge transport properties and functionality of molecule-nanoparticle ensembles

Devid, E.J.

6

Spin transition in arrays of gold nanoparticles and spin crossover molecules

We investigate if the functionality of spin crossover molecules is preserved when they are assembled into an interfacial device structure. Specifically, we prepare and investigate gold nanoparticle arrays, into which room-temperature spin crossover molecules are introduced, more precisely $[Fe(AcS\text{-}BPP)_2](ClO_4)_2$, where AcS-BPP = S-(4-{[2,6-(bipyrazol-1-yl)pyrid-4-yl]ethynyl}phenyl)ethanethioate (in short $Fe(S\text{-}BPP)_2$). We combine three complementary experiments to characterize the molecule-nanoparticle structure in detail. Temperature-dependent Raman measurements provide direct evidence for a (partial) spin transition in the $Fe(S\text{-}BPP)_2$-based arrays. This transition is qualitatively confirmed by magnetization measurements. Finally, charge transport measurements on the $Fe(S\text{-}BPP)_2$-gold nanoparticle devices reveal a minimum in device resistance versus temperature, $R(T)$, curves around 260-290 K. This is in contrast to similar networks containing passive molecules only, that show monotonically decreasing $R(T)$ characteristics. Backed by DFT calculations on single molecular conductance values for both spin states, we propose to relate the resistance minimum in $R(T)$ to a spin transition, under the hypothesis that 1) the molecular resistance of the high-spin state is larger than that of the low-spin state, 2) transport in the array is governed by a percolation model.

This chapter is based on the article published in ACS Nano, **9**, (2015), 4496-4507.
Spin Transition in Arrays of Gold Nanoparticles and Spin Crossover Molecules,
E. J. Devid, P. N. Martinho, M. V. Kamalakar, I. Šalitroš, Ú. Prendergast, J.-F. Dayen, V. Meded, T. Lemma, R. González-Prieto, F. Evers, T. E. Keyes, M. Ruben, B. Doudin and S. J. van der Molen.

6.1 Introduction to molecular complex-nanoparticle ensembles

One of the most exciting prospects of molecular electronics is that future nanoscopic devices may be based on molecules with a well-defined functionality. Among the most prominent examples are molecular rectifiers [1, 2] and switchable molecular devices [3-6]. Indeed, molecular switches based on a variety of mechanisms have been considered for applications. These include mechanically interlocked switches (rotaxanes, catenanes), photochromic molecules (diarylethenes, diazobenzenes), tautomerization switches and redox-active molecules. To drive switching at the device level typically requires molecular assembly at a solid interface (i.e. electrodes). *A priori*, it is difficult to judge if a switchable molecule will retain its function once it is inserted in a metal-molecule-metal device. Connecting electrodes to a molecule may affect the molecule´s mechanical freedom, alter its precise density of states and/or influence the decay of the excited state initiating the switching process. Nevertheless, a growing number of proof-of-principle switchable devices, based on bistable molecules, have been presented in literature [6]. Here, we concentrate on molecules with a bistability related to the other basic property of the electron besides charge, i.e. its spin. Specifically, spin crossover (SCO) molecules are studied, with the aim of finding a signature of molecular spin transition in an interfacial device geometry.

SCO molecules generally consist of a central transition metal ion, coupled to organic ligands [4, 5, 7]. Depending on the specific geometry and the strength of the ligand field, such molecules may switch between a diamagnetic, low-spin (LS) and a paramagnetic, high-spin (HS) state as a function of temperature, illumination, pressure, magnetic or electric field [8-15]. To illustrate this principle, Figure 6.1 shows the molecular species synthesized for this study *[Fe(AcS-BPP)$_2$](ClO$_4$)$_2$* (where *AcS-BPP* denotes *S-(4-{[2,6-(bipyrazol-1-yl)pyrid-4-yl]ethynyl}phenyl)ethanethioate*).

Basically, a rod-like metal complex is displayed, based on an iron (II) ion and two organic ligands [16]. In bulk powder form, the formula is [Fe(AcS-BPP)$_2$](ClO$_4$)$_2$ (hereafter called molecule **1**) including thioacetate protecting groups and counter ions. After exposure to gold surfaces, deprotection of the Ac-S anchor groups occurs, leading to a formal composition of Fe(S-BPP)$_2$ under near surface conditions (hereafter called molecule **1'**).

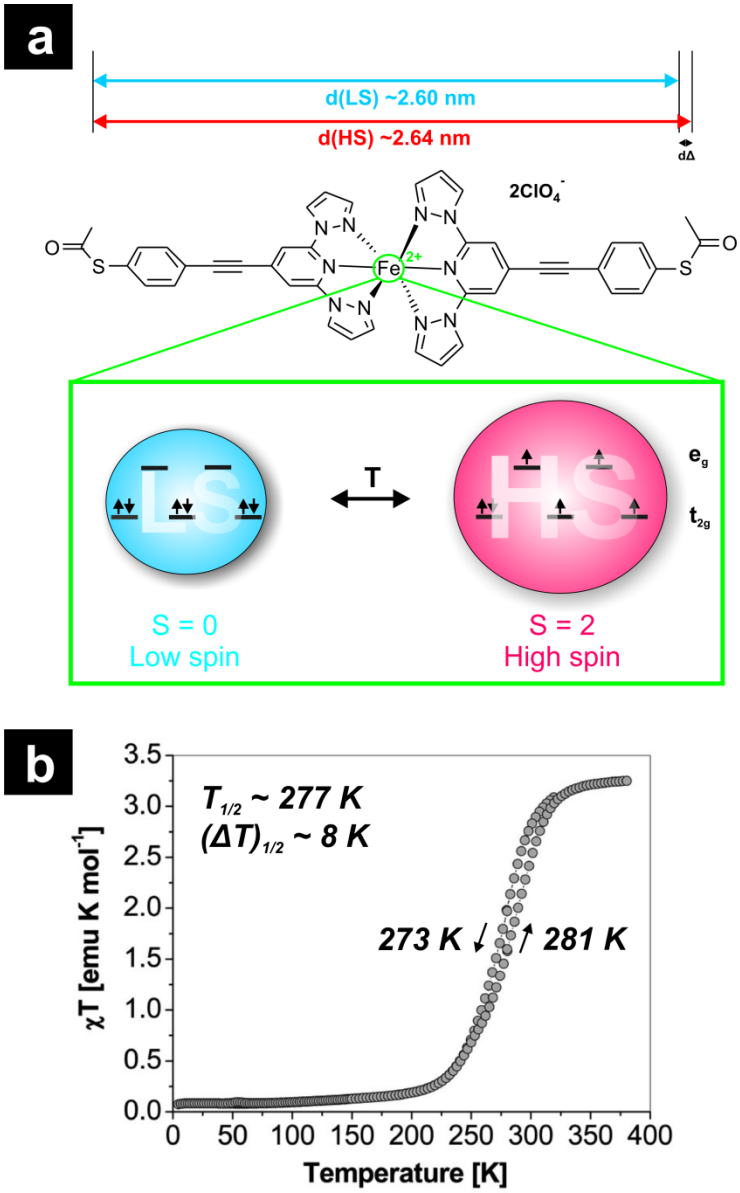

Figure 6.1: Spin crossover molecule **1**: (a) Schematic representation of molecule **1** visualizing its spin transition (governed by the occupancy of the t_{2g} and e_g states) and the corresponding tiny length change. (b) Temperature-dependent magnetic susceptibility measurement of the same bulk crystalline SCO compound. The spin transition temperature is centered at $T_{1/2}$ = 277 K and accompanied by a thermal hysteresis loop with $\Delta T_{1/2}$ = 8 K.

The bulk sample of **1** exhibits a spin transition as illustrated by a measurement of the magnetic susceptibility χT. Plotting χT versus temperature T indicates a broad, but distinct, transition between a S = 0 (diamagnetic) and a S = 2 (paramagnetic) state, see Figure 6.1(b). Moreover, the transition is hysteretic due to intermolecular interaction ('cooperativity') in the bulk lattice [7].

While SCO compounds have been synthesized and studied in bulk since the 1930s [8, 9], the research activity in this field has intensified in recent years. On the one hand, prospective applications motivate scientists to increase the transition temperature up to ambient by synthesizing new molecules [17, 18]. On the other hand, decreasing the size of the molecular system from macroscopic (bulk) down to the nanometer scale can provide unique insight into fundamentals of spin transition properties, with applications to nanoelectronics and spintronics. The switching properties of SCO compounds may be strongly modified at the nanoscale, however. It is known that the characteristics of SCO compounds depend critically on the identity of the transition metal ion, the nature of the ligands and the exact symmetry and strength of the ligand field [19, 20]. Clearly, some of these properties may change drastically when decreasing the dimensions of ensembles of SCO molecules and their environment. Recently, scanning tunneling microscopy (STM) experiments performed on ultra-thin films at low temperatures revealed that electric field-induced switching can only occur in the second molecular layer [21] or for molecules electronically decoupled from the substrates [22]. Even though the interpretation of STM images is challenging, there are experimental indications that SCO ultra-thin films exhibit transition properties deviating significantly from the bulk, in particular by exhibiting co-existence of HS and LS states at low temperatures [23]. Molecular devices at low temperatures involving a single or a few SCO molecules were also reported by Meded *et al.*, who used a gate-controlled three-terminal molecular device to reveal possible voltage-induced switching [15]. In addition, surface spectroscopy techniques (XAS, UPS, IPES) are well-suited to characterize ultra-thin films. While these ensemble-based techniques are challenged by detection sensitivity issues, they do allow for temperature-dependent studies. M. Bernien *et al.* [24] showed that sub-monolayer films with small energy coupling with the substrate preserved the bulk properties. Furthermore, Zhang *et al.* [25] reported that the substrate ferroelectric state can constrain the stable state of SCO films of several nanometers thick and recently photothermal switching of Fe^{2+} spin crossover@silica-

gold nanocomposites was reported [26]. Finally, Warner *et al.* [27] performed X-ray absorption spectroscopy on submonolayers of iron-complexes on flat Au(111). They found evidence for both a light- and temperature-induced spin transition, but only for a fraction of the molecules. The authors argue that the precise molecular behaviour depends sensitively on the interactions with the surface and with other molecules.

Overviewing scientific literature, the question as to if and how spin transition persists in nanoscale ensembles remains open, with strong experimental indications that interactions with the substrates, or connecting electrodes, play a decisive role in the preservation or not of spin transition. Since this issue is of fundamental importance, validating the occurrence of a SCO transition is key if we want to use this type of molecule in functional devices. We propose the following two criteria for convincing experiments:

- the experimental insight should not rely on a single technique only. In other words, the electrical transport properties should be complemented by other methods, validating in particular the occurrence of a spin transition and (ideally) providing structural insight into the interaction of the SCO molecules to the substrate.
- temperature-dependent studies must be performed. Temperature is the best indicator of thermodynamic stability of a given phase, probing the cooperativity of the system, and providing a direct comparison with known bulk properties. Previous experimental approaches to SCO molecular transport provided limited insight into temperature dependence, and most published results investigate switching of SCO molecules through a stimulus (electric field) undocumented for thin films or bulk materials.

The aim of this present work is therefore to perform temperature-dependent studies of the transition behaviour of SCO molecular device structures, combining Raman spectroscopy, magnetometry, and electrical transport measurements, complemented by charge transport calculations.

We make use of two-dimensional (2D) arrays of molecular-bound Au nanoparticles, bridging the gap separating the molecular length scale and typical length scales of patterned metallic electrodes. As a basic structure, we use samples made of alkanethiol-protected gold nanoparticles. With an exchange process based on self-assembly, the molecules **1** (Figure 6.1) are inserted onto and between the nanoparticles. In this way,

an ensemble is created based on single nanoparticle-molecule-nanoparticle junctions [28-31]. The arrays thus prepared are structurally robust at room temperature, capable of withstanding temperature sweeps, and easily addressable by external stimuli. Moreover, they allow for (control) experiments to check the device properties before and after molecular insertion. These may include several varieties of optical spectroscopy, representing an important advantage over true single-molecule techniques. At a density of junctions on the order of 10^4 per μm^2, the device architecture chosen provides direct statistical information on molecular junction properties. Still, as in most molecular device geometries, it is difficult to know the exact number of molecules involved in a single nanoparticle-molecule(s)-nanoparticle unit.

This Chapter is organized as follows. After introducing sample preparation and basic experimental methods, we describe and discuss temperature-dependent Raman spectroscopy and magnetization measurements, respectively. These give evidence for a (partial) spin transition in arrays containing SCO molecules. Next, we present conductance experiments as a function of temperature, followed by single-molecule transport calculations. Finally, we show that the experimental conductance data are consistent with the combined Raman and magnetization results and with transport calculations. For this, we employ a simple percolation model that incorporates a temperature-dependent (partial) spin transition.

6.2 Experimental method of a spin crossover-gold nanoparticle array

The method for the fabrication of molecule **1'**-gold nanoparticle arrays is described in detail in the paragraph 3.3.1. In short, spherical gold nanoparticles (8.5 ± 1.5 nm diameter) are synthesized in-house and modified with octanethiol molecules [16, 32]. Next, they are made to self-assemble in an ordered array on a water surface. Such an array can be transferred to a substrate of choice by microcontact printing. For this study, we used glass, quartz and Si-SiO_2 substrates. Furthermore, we have transferred arrays to high-aspect-ratio nanotrench devices [16, 33, 34]. The latter are made by electron-beam lithography and consist of two wide electrodes (typical widths are ≈ 20 μm) that are separated by only ~100 nm, so as to define a favourable aspect ratio. Figure 6.2 shows a SEM (scanning electron microscopy) micrograph and a schematic of a typical

device (see also Appendix C.1). In some cases, multiple stamping is performed to create layer-on-layer molecule-gold nanoparticle network devices. 'Virgin' networks of octanethiol-covered gold nanoparticles are first characterized via charge transport measurements and UV-Vis absorption spectroscopy. Subsequently, molecular exchange is performed by inserting a sample in a solution of **1** in acetonitrile (MeCN).

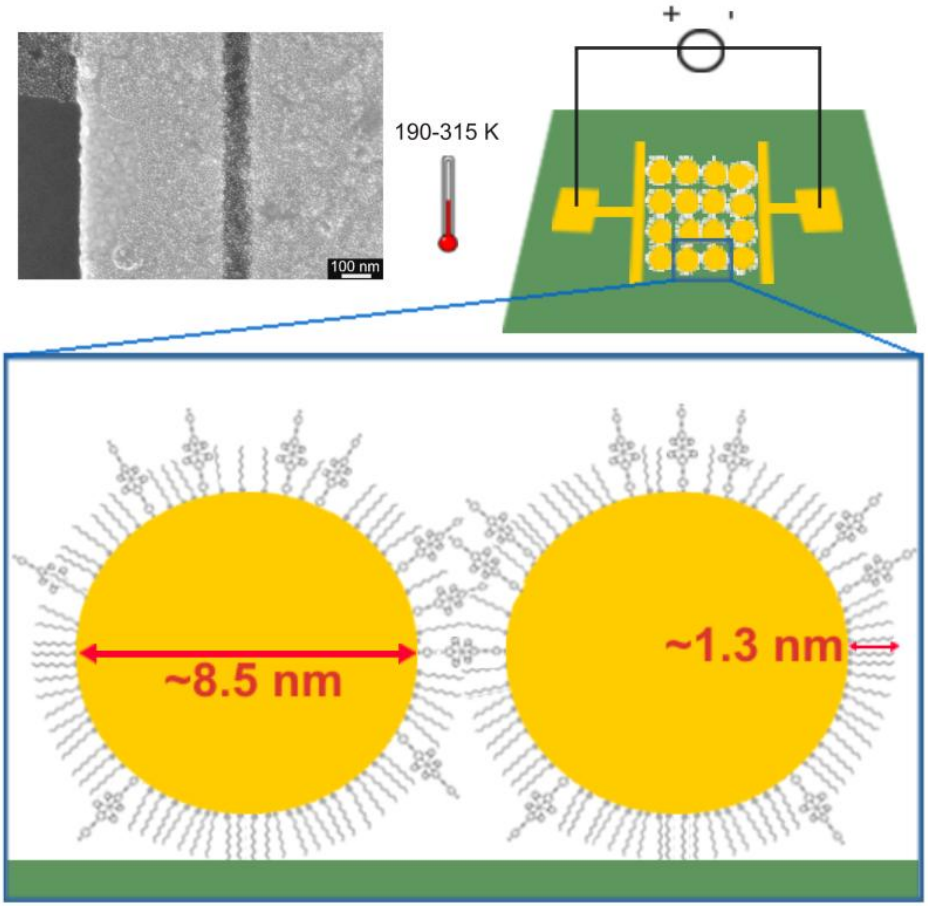

Figure 6.2: Micrograph (top left, SEM image: scale bar is 100 nm) and a schematic representation (top right) of a 2D molecule-gold nanoparticle array device (in reality, the gold nanoparticles are ordered in a triangular lattice). Bottom: schematic representation of a gold nanoparticle-molecules **1'**/C8 molecules-gold nanoparticle junction on an insulating substrate, where **1'**/C8 denotes a mixture of molecules **1'** and octanethiols.

UV-Vis spectroscopy is used to determine if the molecular exchange process was successful. In the latter case, the surface plasmon resonance (SPR) peak of the initial octanethiol-gold nanoparticle array shows a red shift after exchange, attributed to the increase in the dielectric constant experienced by the nanoparticles (see Appendix C.2). In our study, we combine charge transport experiments with Raman spectroscopy and magnetization measurements. All three sets of experiments are performed as a function of temperature. Due to practical constraints, these experiments have been performed on different samples, all prepared in an identical manner. Finally, we note that sets of reference samples have been prepared to benchmark the data on SCO molecules. The first set is based on a similar exchange procedure but with dithiolated OPE (oligo(phenylene ethynylene)) molecules instead of the deprotected SCO complex molecules **1'**. For the second set, the non-metallated ligand S-BPP (see Chapter 5, Figure 5.1) is used to coat the gold nanoparticles directly, after which array devices are created via self-assembly and microcontact printing [16].

6.3 Temperature-dependent Raman spectroscopy measurements

The arrayed nature of the gold nanoparticles and their small inter-particle separation leads to a plasmon absorbance, which is resonant with the 633 nm light used to excite the samples for Raman spectroscopy. Therefore, the Raman spectrum of the 2D molecule **1'**-gold nanoparticle array is expected to be surface enhanced (so-called surface-enhanced Raman spectroscopy (SERS)). Correspondingly, from comparison of the Raman spectra of the bulk powder of molecule **1** and the 2D molecule **1'**-gold nanoparticle array, it is evident that there are some very significant changes in the relative intensity and the vibrational frequencies of several key modes of the complex on gold nanoparticle binding. This technique, which provides a molecular fingerprint reflecting the structure of the adsorbed species, is ideally suited to detect the dominant SCO phase at a given temperature and provides insight into molecules-surface interactions.

Many of the observed changes are strongly reminiscent of our previous report on binding of the parent S-(4-{[2,6-(bipyrazol-1-yl)pyrid-4-yl]ethynyl}phenyl)thioate (S-BPP) ligand at a gold nanoparticle array [16]. For example, the mode which dominates the SERS spectrum at 1574 cm^{-1} is attributed to the aryl in-plane C-C stretch mode of the benzenethiol moiety which is observed at approximately 1590 cm^{-1} in the unbound

complex [16, 35]. In the Raman spectrum of the SCO complex, this mode is superimposed on a more intense pyridine C-C stretch mode. The frequency shift and dramatic increase in intensity of this benzenethiol mode observed on nanoparticle binding of the SCO complex are analogous to the spectral behaviour observed for the free AcS-BPP when it was bound to a gold nanoparticle array and is strong evidence that the molecule **1'** is thiol-bound to the gold. Indeed, the dramatic relative increase in intensity of the 1574 cm^{-1} mode, along with other benzenethiol modes at 1078 and 406 cm^{-1}, is consistent with the surface enhancement of these signals due to proximity of the associated moieties to the plasmonic field of the nanoparticles, which would be expected if the complex is binding to the nanoparticles through the benzenethiol unit. A new feature evident at 321 cm^{-1} is tentatively attributed to the Au-S mode. Notably, the pyrazine and pyridine modes at 1619 cm^{-1}, 1381 cm^{-1} and 1014 cm^{-1} which dominate the Raman spectra of the bulk **1** powder are considerably weaker compared with the benzenethiol features in the SERS spectrum. Therefore, the overall pattern of surface enhancement of the Raman spectral data indicates that molecule **1'** is thiol-bound and oriented largely normal to the gold nanoparticle surface, as indicated by the absence in comparable SERS enhancement in the pyrazine and pyridine modes.

The temperature-dependent Raman spectra of the bulk powder molecule **1** and the molecule **1'**-gold nanoparticle array were then compared over the temperature range 353 to 80 K, which encompasses the SCO transition in the bulk powder. The full temperature-dependent Raman spectra of the bulk SCO powder **1** are shown in Figures C-3 till C-5 in Appendix C.3. They are strongly reminiscent of Raman spectral changes accompanying spin transition of a related iron complex [17]. Indeed, similar key markers of spin transition are observed. Most notably, in going from room to low temperature, the feature at 1014 cm^{-1} disappears and is replaced by a mode at 1039 cm^{-1}. From DFT calculations, the peak at 1014 cm^{-1} is attributed to a pyridine ring breathing mode whose motion is coupled strongly to the Fe(II)-N stretch. Correspondingly, the replacement feature at 1039 cm^{-1} is attributed to the analogous normal mode in the LS state. The intensity of the feature at 1014 cm^{-1} (integrated against a relatively temperature independent mode at 1590 cm^{-1} from benzenethiol) is plotted against temperature in the inset of Figure C-4 in Appendix C.3. This plot yields a sigmoidal curve that exhibits a transition temperature in excellent agreement with the magnetization data for bulk powder (see Figure 6.1(b)). This result indicates that these Raman spectral changes can be attributed to spin transition. In addition, C-C stretch

modes for the pyridine and pyrazine ligands respectively at 1589 cm^{-1} and 1618 cm^{-1} change in relative intensity and shift to higher energy with decreasing temperature, consistent with strengthening of these bonds as the metal antibonding e_g* levels are vacated in the LS state of the SCO complex.

The influence of changing temperature on the SERS spectrum of the spin transition molecule **1'** in the nanoparticle array (i.e. 2D molecule **1'**-gold nanoparticle array) is less dramatic. This is a result of the domination of the SERS modes of the benzenethiol which is not strongly influenced by temperature. Nonetheless, close inspection of modes associated with the iron complex show that clear spectral changes occur with temperature in **1'**-gold nanoparticle arrays, as displayed in Figure 6.3 (see also Appendix C.4, Table 1 and Figure C-6). Most tellingly, the major spectral changes occur between approximately 800 and 1200 cm^{-1} where, from DFT calculations, the majority of the coupled ligand breathing/Fe-N vibrations occur. In particular, the band at 1014 cm^{-1}, identified as a marker of spin transition in the bulk material, decreases significantly at low temperature. In parallel, a feature at 1104 cm^{-1} increases in intensity. This mode is tentatively assigned to the LS state ligand ring breathing coupled to Fe(II)-N bonds seen at 1039 cm^{-1} in the bulk SCO compound **1**, keeping in mind that unambiguous assignment of this mode is not possible without accompanying DFT calculations of the nanoparticle bound complex. We note that, in addition, a weak feature at 1125 cm^{-1} decreases with decreasing temperature with concomitant grow-in of a feature at 1151 cm^{-1}. On the basis of DFT calculations, both are attributed to in-plane ring NCH stretch modes coupled to equatorial Fe-N stretch in the LS state. Interestingly, the alkyne C≡C stretching mode at 2207 cm^{-1} shifts to the blue by approximately 8 cm^{-1} at low temperature and sharpens significantly. Such behaviour was observed previously in experiments where S-BPP-ligand were incorporated in the nanoparticle arrays (i.e. S-BPP-gold nanoparticle array), in the absence of iron [16], and therefore this is not related to spin transition. It is important to note that some of the features observed in the molecule **1'**-gold nanoparticle array did not resolve in the bulk SCO material. This can be attributed to surface binding and SERS effect which are expected to change both the selection rules and intensities of the modes observed.

All in all, evidence from Raman spectroscopy for persistence of spin transition in the gold nanoparticle bound metal complex is compelling, but the fact that the Raman spectral features associated with the low-spin and high-spin states are not completely

lost at the most extreme temperature suggests that the transition is not as complete as was observed in the bulk.

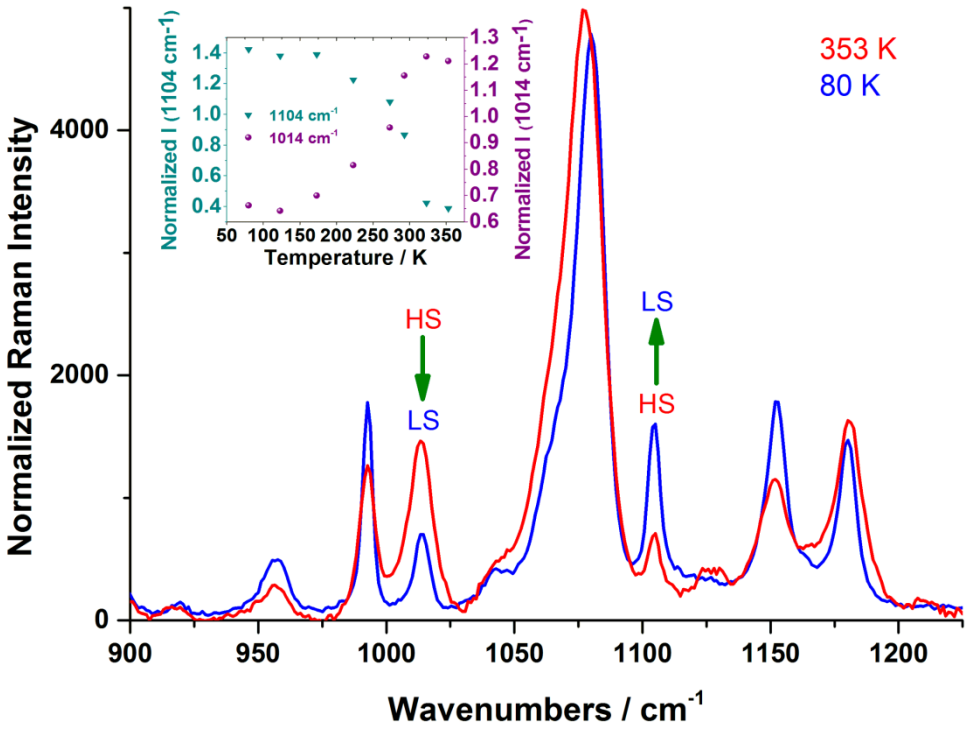

Figure 6.3: Raman spectra of a 2D molecule **1'**-gold nanoparticle array at 353 and 80 K, respectively, excited at 633 nm (incident power 1.2 mW at the array) on a quartz substrate. Note that the mode at 1014 cm^{-1} increases with increasing temperature, whereas the mode at 1104 cm^{-1} decreases. Inset shows more detail on the intensity of these two modes, which are sensitive to the spin transition, as a function of temperature. Both modes are normalized to the 406 cm^{-1} benzenethiol mode which showed weak temperature dependence.

To provide better quantitative insight, the intensity of both the 1014 cm^{-1} and 1104 cm^{-1} modes, which are markers of HS and LS states in the array respectively, are plotted versus temperature for the normalized spectra (see inset of Figure 6.3). Their intensity values are given relative to a benzene thiol mode, used as a phase-independent temperature marker in the bulk powder. As shown in Figure 6.3 inset, this reveals two sigmoidal curves, one growing in (the HS marker, i.e. 1014 cm^{-1} mode) and one

decreasing (the LS marker, i.e. 1104 cm^{-1} mode), with a midpoint each of around 270 K. This temperature-dependent behaviour correlates well with the magnetic data shown below and is consistently reminiscent of the behaviour of the spin transition in the bulk powder [19]. The slope of the temperature dependence, weaker in the 2D molecule **1'**-gold nanoparticle array than in the bulk powder, may be attributed to the fact that a pure HS state is not completely achieved over the temperature range explored here, as indicated by residual features from the HS state at low *T* and vice versa. From the relative change to the integrated area under the features at 1014 and 1104 cm^{-1}, we can estimate what fraction of the SCO molecules undergoes spin transition, however, with significant uncertainty. The percentages we find are 65% (from 1014 cm^{-1} mode) and 80% (from 1104 cm^{-1} mode), respectively. The differences in the estimated areas are attributed to residual uncorrected background in the Raman spectra which is stronger under the 1014 cm^{-1} band. We can say therefore that we obtain a minimum of 65% spin transition. It is important to note that the temperature-dependent changes to the Raman spectra of both the SCO bulk powder **1** and molecule **1'**-gold nanoparticle array were fully reversible on restoring temperature to its original value. We do not find experimental indications of hysteresis in the spin transition, i.e. the temperature sweeping direction does not matter.

We have benchmarked our findings on SCO transition by also performing temperature-dependent Raman on the reference C8-gold nanoparticle array (see Chapter 5, Figure 5.8). In contrast to the SCO spectra, little spectral change and no indication of transition are observed in the temperature-dependent data: besides broadening out of features at high temperatures with an increase of the background, no clear shifts are observed in the few bands that are attendant in Figure 5.8.

In summary, temperature-dependent Raman spectroscopy provides evidence for a spin transition in the molecule **1'**-gold nanoparticle arrays and reveals that the molecules are bound to Au with their thiol group(s). However, unlike the bulk material, the transition does not appear to be complete, with a minority of the molecules not exhibiting a crossover.

6.4 Magnetization measurements

Magnetic properties have been investigated to confirm the occurrence of a spin transition in the nanoparticle array. Three samples are prepared by layer-on-layer

deposition of C8-gold nanoparticles arrays onto quartz substrates of 10 x 6 mm size. Two of these samples are then exchanged with SCO molecules. The total magnetic moment of gold nanoparticle networks incorporating molecules **1'** (i.e. spin transition samples **B** and **C** (each sample contains different amounts of nanoparticles due to stamp size variation ect.) as well as a reference sample **A** (containing octanethiols only) have been measured on a SQUID magnetometer (see Appendix C.5) under applied magnetic field of 1 T, in the temperature range 90-400 K (see Figure 6.4).

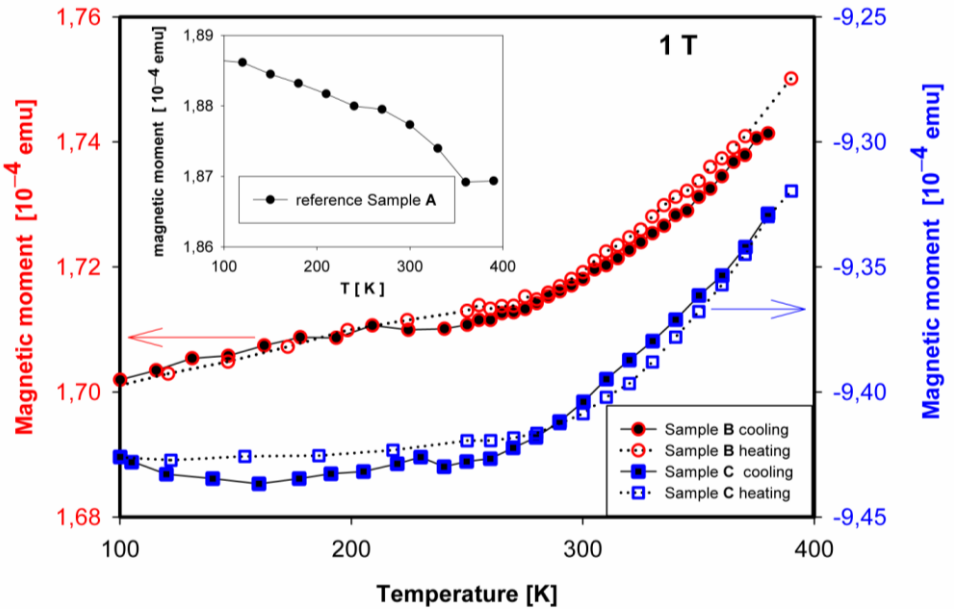

Figure 6.4: Temperature-dependent magnetization measurements on three gold nanoparticle network samples (on quartz substrates). For gold nanoparticle networks incorporating molecules **1'** (samples **B** and **C**), a clear change in magnetic moment is observed around 250 K, consistent with a partial spin transition. Inset: temperature-dependent magnetic moment of reference sample **A**, which contains a gold nanoparticle network with only octanethiol molecules. All magnetic measurements were carried out under a 1 T external magnetic field. (These experiments were performed by Dr. I. Šalitroš at the Institute of Inorganic Chemistry, Technology and Materials in Bratislava.)

All three samples contain predominantly diamagnetic material (quartz substrate, gold nanoparticle and octanethiol (C8)). A diamagnetic signal is indeed detected for sample **C**. Because the diamagnetic response of samples **A** and **B** is most probably weaker than

the signal coming from the nearby background signal environment of the sample position (tape and quartz), the signal is found to be paramagnetic for samples **A** and **B**.

In Figure 6.4, for the temperature range 100-200 K, the magnetic moment of both **B** and **C** samples remains rather constant whereas it rises with increasing temperature in the 200-400 K range. Both curves show similar temperature-dependent behaviour, indicating reproducibility. The reference sample **A** shows a different behaviour, with magnetic moment diminishing with increasing temperatures. One can therefore tentatively attribute the increase of paramagnetism with temperature for samples **B** and **C** to the occurrence of a diamagnetic-paramagnetic spin transition. Consistent with the Raman data, measurements in both cooling and heating directions confirm the temperature reversibility.

The lack of an abrupt spin transition with temperature is attributed to the diluted nature of SCO switching centers in the sample leading to diminished cooperativity and the absence of saturation at 400 K for nanoparticles samples confirms the partial nature of the spin transition [36, 37].

While care must be taken in the magnetic data interpretation due to the limited signal from the molecules of interest, the findings confirm the outcome of Raman data, with indications of a spin transition in nanoparticles arrays if molecules **1'** are present, at temperatures comparable to those found on bulk SCO powders. The persistence of a spin transition in the networks opens the possibility to create a macroscopic device providing insight into the influence of the transition at the molecular level on electrical properties.

6.5 Charge transport experiments

We have performed conductance measurements as a function of temperature on four types of samples, all made of molecular-bound nanoparticles arrays. Three are reference samples, containing 'passive' molecules only (octanethiols, OPE-dithiols and monothiolated 'S-BPP', i.e. the uncoordinated ligand AcS-BPP used in the molecule **1** in Figure 6.1(a)) [16]. For all of these, no transition is expected to occur with temperature. Hence, they provide reference temperature-dependent transport properties, to be compared to the fourth sample type, which incorporates molecule **1'**. Figure 6.5(a) shows the low-bias resistance R versus temperature T for a C8-gold nanoparticle

network (stamped three times, yielding 1-2 monolayers: see caption for details). Interestingly, for this 'virgin' molecular device, a monotonically decreasing curve is observed that plateaus at higher *T*. We note that the alkanemonothiols form a tunnel barrier between neighbouring nanoparticles. Transport through such a barrier is expected to be virtually temperature-independent. Hence, the temperature-dependence observed in Figure 6.5(a) must be related to the properties of the nanoparticles. Indeed, it is a result of Coulomb blockade: due to the small size of the gold nanoparticles, a finite energy is required to add one electron to a nanoparticle. This 'charging energy' E_C is connected to a nanoparticle's capacitance C and the electron charge e via $E_C = e^2/2C$. Upon cooling the sample, the thermal energy k_BT can become lower than E_C. As a result, transport is increasingly blocked (Coulomb blockaded), and the resistance increases dramatically. This effect has been well-studied in networks, by us and others [16, 29, 34, 38, 39].

Figure 6.5(b) shows *R* versus *T* for a network sample (three times stamped) into which C8 molecules have been exchanged with OPE-dithiol bridges. Clearly, the presence of the conjugated OPE rods has led to a much lower device resistance. Qualitatively, however, the *R*(*T*) behaviour has not changed. Again, a monotonically decreasing curve is seen, with characteristics that are dominated by Coulomb blockade in the nanoparticles [34, 40].

For arrays and networks containing spin crossover molecules **1'**, however, the results can be very different. Figure 6.5(c) shows *R* versus *T* for such a sample (three times stamped). In contrast to Figure 6.5(a) and Figure 6.5(b), the *R*(*T*) plot in Figure 6.5(c) shows an upturn. This results in a rather shallow minimum, roughly stretching between 260 and 290 K. In addition, Figure 6.5(d) shows a *R*(*T*) plot for a sample on which stamping was done only once, resulting in an imperfectly ordered single nanoparticle layer. Although this yields a much higher overall resistance value, the *R*(*T*) curve remains qualitatively similar to the one in Figure 6.5(c). Indeed, both Figure 6.5(c) and Figure 6.5(d) exhibit a clear minimum. This behaviour not only differs fundamentally from Figure 6.5(a) and Figure 6.5(b) but also from our third reference systems, i.e. networks containing the monothiolated S-BPP. In the latter, the Fe^{2+} ion, which is key to the spin transition, is not present. For such samples, we find that *R* decreases monotonically with increasing *T* without showing a minimum (see Chapter 5, Figure 5.9(a) and Ref. [16] for more details). Hence, the combination of all measurements suggests that the resistance minimum in Figure 6.5(c) and Figure 6.5(d) is intimately

related to the presence of SCO molecules and, specifically, to a temperature-dependent spin transition.

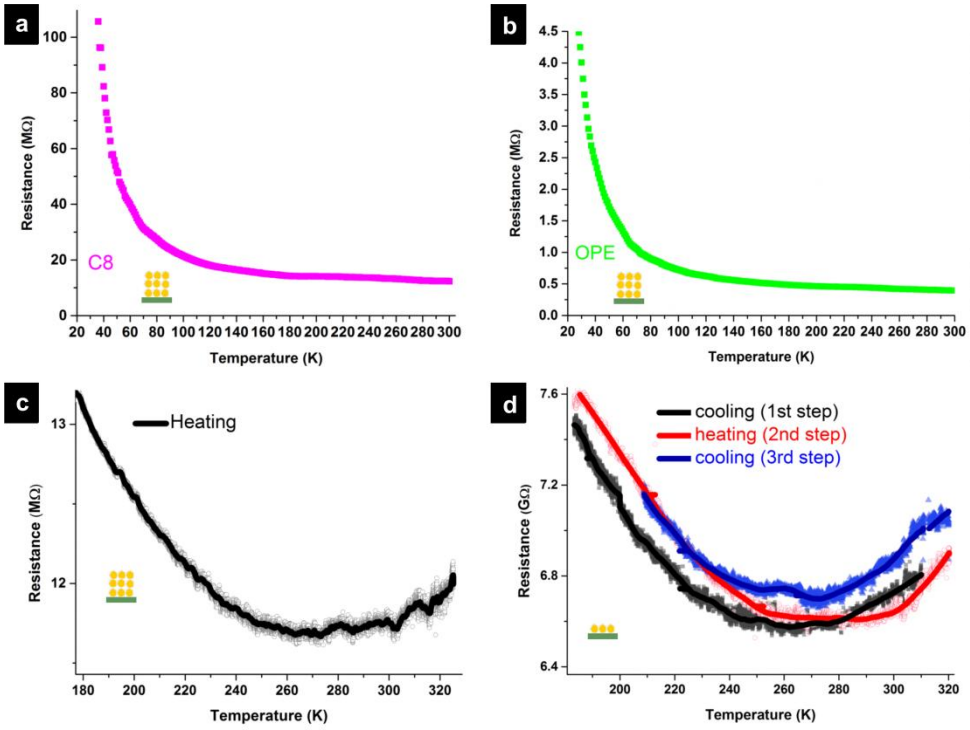

Figure 6.5: (a) Resistance versus temperature (*R*-*T*) measurement of a C8-gold nanoparticle network (stamped 3 times). (b) *R*-*T* measurement of a OPE-gold nanoparticle array (stamped 3 times). (c) *R*-*T* measurement of a molecule **1'**-gold nanoparticle network (stamped 3 times). (d) *R*-*T* measurement of a single layer molecule **1'**-gold nanoparticle array. All resistances are determined at low-bias ($V \leq 0.3$ V) on nanotrench devices [33]. In Figure 6.5(c) and Figure 6.5(d), we show both an averaged curve and (a random 10% part of the) raw data (320 data points per Kelvin). We note that while 4 out of 8 samples with spin transition molecules did exhibit a resistance minimum, also 4 did not (see Appendix C.6). We will come back to that below.

However, before accepting this hypothesis, we should consider an alternative explanation. Recently, Wang *et al.* [41] reported a variation in $R(T)$ behaviour for multilayered arrays of octanethiol-covered Au nanoparticles, dependent on thickness.

For samples containing up to four layers of 7 nm-diameter nanoparticles, they find that $R(T)$ plots shows a monotonic decrease. From five layers upwards, however, they observe a resistance minimum, an effect which they explain via a diffusive hopping model. For 13 nm particles, the latter border shifts to three layers. For this reason, it is important to emphasize that our reference samples (not only octanethiol like Wang, but also OPE and bare S-BPP arrays) do not yield a resistance minimum. This is fully consistent with the data set of Wang *et al.*, as our particles are 8.5 ± 1.5 nm in diameter, i.e. close to 7 nm [16]. In contrast, we do observe a resistance minimum for samples that contain spin transition molecules. This is the case not only for triple-stamped samples, but, importantly, also for arrays that were stamped only once (see Figure 6.5(d)).

Hence, our full set of transport experiments, in combination with our Raman and magnetometry data, indicates that a spin transition in the SCO molecules is key to the anomalous $R(T)$ plots observed. If we also assume that the HS state has a higher low-bias resistance than its LS counterpart, as we will discuss below, we have the ingredients to explain the upturn. Upon heating around the transition temperature, more and more molecules will make the transition, and the resistance will increase. Still, Coulomb blockade will play its role too, as the charging energy E_C of the gold nanoparticles in Figure 6.5(c) and Figure 6.5(d) should be similar to the values for Figure 6.5(a) and Figure 6.5(b) (the nanoparticles and samples are made according to the very same procedure). Hence, for the lower temperatures, an increase of R upon cooling is also expected. A combination of Coulomb blockade and a spin transition could thus qualitatively explain the minimum observed in Figure 6.5(c) and Figure 6.5(d).

In the following, we combine DFT calculations of the electrical properties of these molecular junctions with a simple macroscopic percolative network model to provide a better insight into the $R(T)$ findings.

6.6 Theoretical charge transport calculations

Up to now, theory is diverse on predicting how the conductance of SCO molecules would change during spin transition. Baadji *et al.* [42] found a resistance decrease when going from the LS to the HS state (i.e. $R_H < R_L$) for a SCO molecule of their choice. Meded *et al.* [15], on the other hand, predict that the resistance is lowest in the LS state (i.e. $R_H > R_L$), based on experimental findings on molecules more similar to

the ones studied here. One reason for this discrepancy is that two competing effects can play a role upon a LS to HS transition. On the one hand, the energy gap between the frontier orbitals (HOMO-LUMO gap) decreases. This is expected to increase conductance, as the distance from Fermi level to the nearest level will generally decrease as well. On the other hand, the electronic coupling between the ligands at both sides of the Fe^{2+} ion decreases when going from the LS to HS state. In first approximation, the related decrease in wave function overlap should reduce conductance. Hence, it is not *a priori* obvious if one should expect a conductance increase or decrease upon spin transition for a particular type of molecules.

For this reason, we specifically focus on calculating charge transport through molecule **1'** connected to Au leads. We perform simulations of the transmission function by utilizing our in-house developed Non-equilibrium Green's Functions (NEGF) formalism [43, 44] based on Density Function Theory (DFT) input coming from the quantum chemistry package Turbomole [45-47]. The formalism was successfully utilized earlier on a similar class of molecules [48], using BP [49, 50], a standard Generalized Gradient Approximation (GGA) exchange-correlation (XC) functional. Here, however, we use B3LYP [51, 52] as an XC functional to obtain the transmission functions for both the HS and LS state of the molecule **1'** as presented in Figure 6.6.

Upon an, admittedly, rough comparison between experimentally obtained first optical excitations and HOMO-LUMO gaps produced with a few different XC functionals, one directly observes that BP's 0.3 eV is too small (by a factor of 4) when compared to the experimental lowest optical excitation of 1.3 eV [53]. B3LYP on the other hand produces 3.2 eV, a value too high by a factor of 2. $[Fe(TPY)_2]^{2+}$ (with TPY = 2,2′:6′,2″-terpyridine) showed very similar trends compared to molecule **1'** (only slightly smaller) on the calculations side. It is worth noting that agreement across different XC functionals is much better for the LS state where the discrepancies never exceed 50% when compared to the lowest optical excitation of LS of $[Fe(TPY)_2]^{2+}$ found in experiment [54], for details see Table VI in Ref. [15]. We note that the $[Fe(TPY)_2]^{2+}$ complex is not known to switch in experiment [55].

Indeed, we find that the HOMO-LUMO gap in the HS state tends to be smaller than in the LS state for the corresponding XC functional. Consequently, the HS frontier orbitals tend to be closer to resonance with the Fermi level E_F of the junction. From

this, one might expect that the HS conductance exceeds the LS conductance, as anticipated above [54]. Figure 6.6 shows the calculated transmission function versus energy, $T(E)$, for both LS and HS states. The single molecular conductance G at low-bias is related to $T(E)$ by $G = 2e^2/h\ T(E_F)$, where h denotes Planck's constant. Remarkably, although the transport gap in Figure 6.6 is indeed smaller for the HS state, the conductance (transmission) of the LS state is clearly the higher of the two.

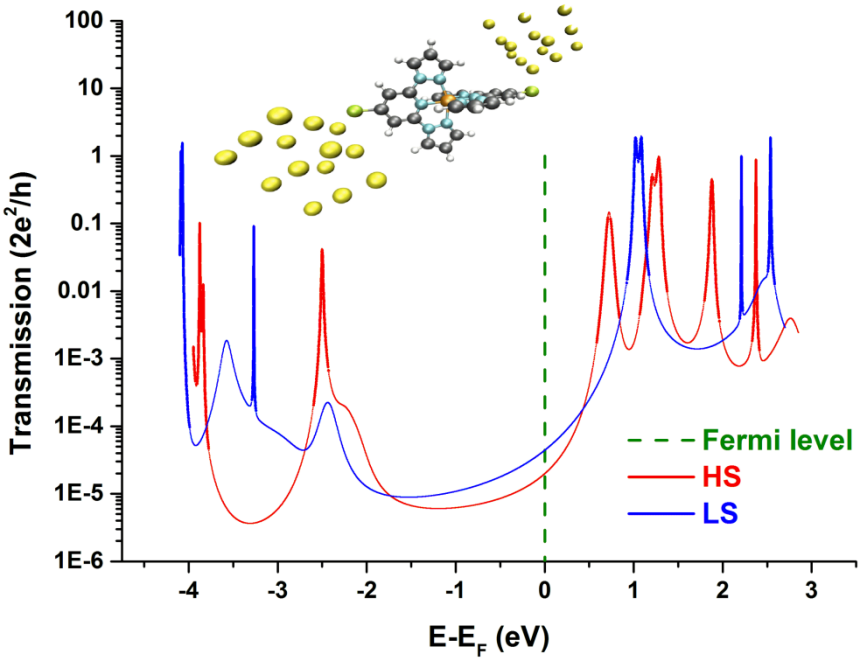

Figure 6.6: Calculated electron transmission probability as a function of energy, $T(E)$, for molecule **1'** in LS (blue curve) and HS (red curve) states. The inset shows the configuration considered (gold atoms are displayed in yellow). The conductance of the LS state is found higher than that of the HS state despite diminishing of the HOMO-LUMO gap upon LS to HS transition. Details of the calculation are described in the paragraph 6.6. (The calculations above have been done by Dr. V. Meded in collaboration with Professor Dr. F. Evers and Professor Dr. M. Ruben).

To understand this, we need to consider inter-ligand coupling as well. From Figure 6.6 we deduce that we dominantly have LUMO transport. Interestingly, the LUMO for these types of molecules is always ligand-based and additionally a ligand wave function has a better opportunity to couple to the gold leads. While spin transition does reshuffle the Fe-states, it does not influence the ligand states as much. Still, it results in

a distance increase between the left and right ligand. The latter makes inter-ligand coupling considerably weaker. In Figure 6.6, we see indeed that the HS LUMO peak (red) is much narrower than the corresponding LS peak (blue). Additionally, the HS Lorentzian peaks well below unity, indicating very asymmetric coupling for the HS state case.

Summarizing, our calculations imply a conductance decrease when going from a LS to a HS state, explained by a reduction in coupling dominating over a decrease in the HOMO-LUMO gap. Keeping in mind differences in HOMO-LUMO gaps that different XC functionals are producing, however, a definite and general answer as to which of the two spin states is better conducting from a theory point of view is still difficult to give. This in itself emphasizes the need for more experimental data.

6.7 Discussion

To relate all of the experimental evidence (Raman and magnetometry results on spin transition) as well as the transport calculations to the $R(T)$ plots in Figure 6.5(c) and Figure 6.5(d), we introduce a pragmatic model. In essence, it describes the influence of a spin transition on the device resistance R via a bond percolation model, assuming $R_H > R_L$ as in the NEGF results (Figure 6.6). Although the model captures the basic physics of our system, we note that it can at most be seen as semi-quantitative.

First, we estimate what percentage of molecules are in the LS and HS states for each temperature T. We choose to do this via a standard approach that captures the essence and allows us to vary parameters. Specifically, we take over the parameters ΔH = 14.3 kJ/mol and ΔS = 55.4 J/mol K, from Šalitroš *et al.* [56] who studied similar spin transition molecules in bulk. In contrast to bulk, however, we assume there is no cooperativity between the SCO molecules in the array. The normalized number of HS molecules x_H is then given by: [7]

$$x_H(T) = \frac{1}{1+exp\left[\frac{\Delta H}{R_B}\left(\frac{1}{T}-\frac{1}{T_{1/2}}\right)\right]}, \qquad (6.1)$$

Where $R_B \equiv N_A \cdot k_B$ is the gas constant (N_A is Avogadro's number). Note that for any finite $T_{1/2}$, $x_H(T)$ does not fully reach unity for $T \to \infty$ in equation 6.1, although for our parameters it does get to 0.998.

Next, we use a percolation model to calculate the total resistance of a 2D array, taking Coulomb blockade into account as well. For this, we first make the pragmatic assumption that the resistance of a single molecule-nanoparticle junction within an array is given by $R_{H\,(L)} = R^{\infty}_{H\,(L)}\ e^{\frac{E_C}{k_B T}}$, where R^{∞}_{H} and R^{∞}_{L} denote the single molecule resistance for the high-spin (H) and low-spin (L) states, respectively, if there were no Coulomb blockade. We use the following normalized values: $R^{\infty}_{H} = 1 = 2 \cdot R^{\infty}_{L}$, inspired by our calculations in Figure 6.6. Furthermore, we assume that the charging energy of the nanoparticles E_C does not depend on the spin state of the molecule. (We use E_C/k_B = 200 K, in correspondence with typical values for octanethiol and OPE networks) [34].

To take percolation into account, we need to properly relate the device resistance R to x_H. Bond percolation displays the relation between the conductivity of the molecules (i.e. the bonds) that bridge the gold nanoparticles in an array and the path to be taken through the bonded array from the source electrode to the drain electrode. In equation 6.2, x_H represents the bridging ratio of high-spin molecules (bridging between the gold nanoparticles junction) divided by the total amount of molecular bridges. If the molecules are randomly placed in between the gold nanoparticles you can predict the probability that a pathway exists in the array related to the bridging ratio. The ratio at which the first pathway is possible (statistically) is called the percolation threshold. For a hexagonal 2D array the percolation threshold is around 35% of all possible molecular bridged junctions.

For this, we make use of a model by McLachlan, which has successfully been applied to molecule-nanoparticle arrays in literature [40]. This type of bond percolation model allows us to describe the influence of the spin crossover molecules on the resistance of the **1'**-gold nanoparticle array. It yields the following implicit equation (see equation 6.2) for the array conductance $G(x_H) = 1/R(x_H)$:

$$\frac{(1-x_H)\left(G_L^{3/4}-G^{3/4}\right)}{G_L^{3/4}+A_c G^{3/4}} + \frac{x_H\left(G_H^{3/4}-G^{3/4}\right)}{G_H^{3/4}+A_c G^{3/4}} = 0, \qquad (6.2)$$

We set $G_H = \frac{1}{R_H}$ and $G_L = \frac{1}{R_L}$ and $A_c = (1\text{-}p_c)/p_c$ where p_c denotes the percolation threshold, coming from the low conductance side. For a hexagonal network, we have p_c

= 2 · sin(π/18) = 0.347, so that A_c = 1.88 [57-61]. With these ingredients, we are ready to calculate $R(T) = R(x_H(T); T) = R\big(x_H(T)\big)\, e^{\frac{E_c}{k_B T}}$.

Figure 6.7(a) shows the result (see black curve). For a system exhibiting a nearly full (99.8%) spin transition, we find that the array's $R(T)$ plot decreases to a minimum, goes up again and slowly goes down to flatten off. The minimum has a depth of up to a few ten % and is found around 220 K.

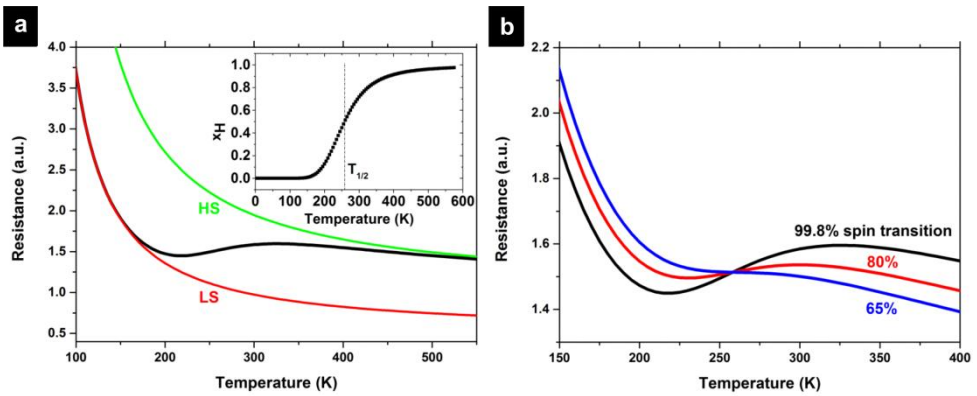

Figure 6.7: (a) General shape of *R*-*T* plot (black) calculated by a percolation network model (see paragraph 6.7). It assumes a spin transition without cooperative effects. A minimum is found for a nearly full spin transition, consistent with Figure 6.5(c) and Figure 6.5(d). The minimum can be rationalized as a transition between two $R(T)$ curves: one for the case that there were LS molecules only (red curve) and one for the case of only HS molecules (green curve). The HS molecules are assumed to have twice the resistance of the LS, consistent with DFT calculations (Figure 6.6). Inset: normalized number of molecules in the high-spin state, x_H versus T as used in the percolation model (see paragraph 6.7, parameters: $\Delta H/\Delta S = T_{1/2}$ = 258 K and ΔH = 14.3 kJ/mol [56], resulting in a 99.8% transition). (b) Calculated $R(T)$ curves if spin crossover is incomplete: 65% (blue curve) or 80% (red curve). The black curve is the same as for (a). The resistance minimum remains for the 80% transition, but disappears near the percolation threshold.

This is qualitatively in agreement with our $R(T)$ data in Figure 6.5(c) and Figure 6.5(d). It is instructive to compare this curve to the plot expected if there were no spin transition at all, i.e. if there were HS molecules only (described by $R_H = R_H^{\infty}\ e^{\frac{E_c}{k_B T}}$, see

green curve in Figure 6.7(a)), or LS molecules only (given by $R_L = R_L^{\infty}\ e^{\frac{E_C}{k_B T}}$, see red curve in Figure 6.7(a)), respectively. Clearly, at low temperatures the model's black curve follows the LS line, whereas it moves to the HS curve as the spin transition takes place. Since $R_H^{\infty} > R_L^{\infty}$, a minimum quite naturally appears.

The red and blue curves show *R* versus *T* for 80% and 65% spin transition, respectively, following the estimates from our Raman data. Comparing the curves, we see that a minimum is still there for the 80%-transition. For the 65%-case, which is near the percolation threshold (coming from the LS state side), the minimum has just disappeared, however. This is consistent with the fact that 4 out of 8 samples did not exhibit a resistance minimum. It shows how sensitive the presence of a resistance minimum is to the extent of the transition, i.e. details of sample preparation will clearly be crucial to observe a resistance minimum.

For instance, if molecular exchange is incomplete and/or if less than 65% of the molecular junctions are able to switch, a minimum is not anticipated.

All in all, the *R*(*T*) data in Figure 6.5(c) and Figure 6.5(d) are qualitatively consistent with the Raman data, magnetometry measurements and transport calculations, assuming that the transition involves more than about 2/3 of the molecules.

6.8 Conclusions

In summary, we have experimentally studied the properties of gold nanoparticle arrays incorporating spin crossover molecules. Raman spectroscopy provides evidence for a (majority) spin transition in these arrays, as qualitatively confirmed by magnetization measurements. The Raman data indicate that molecular binding to gold occurs via benzenethiol termini. Still, it does not appear that the proximity and binding to the metal quenches the spin transition. Resistance versus temperature curves for arrays containing SCO molecules exhibit a pronounced minimum that we do not find in networks containing non-switching, passive molecules only. This resistance minimum can be explained via a percolation model that assumes a spin transition with the HS state being more resistive than the LS state. The latter is in agreement with charge transport calculations presented following the NEGF method.

Even though the electrical signature of a spin transition is not spectacular in our case, the proposed model provides a guideline to pinpoint the occurrence of a spin transition

with temperature in an electrical device. Our work thus demonstrates that proof-of-principle molecular devices based on the spin crossover phenomenon can be designed.

6.9 References

1. A. Aviram and M. A. Ratner, Molecular Rectifiers, *Chem. Phys. Lett.*, **29**, (1974**)**, 277-283.
2. R. M. Metzger, Unimolecular Electrical Rectifiers, *Chem. Rev.*, **103**, (2003), 3803-3834.
3. B. L. Feringa, *Molecular Switches*, Eds.; Wiley-VCH.: Weinheim, June **2001**.
4. P. Gütlich and H. A. Goodwin, Spin Crossover in Transition Metal Compounds I, *Top. Curr. Chem.*, **233**, (2004).
5. M. Ruben, J. Rojo, F. J. Romero-Salguero, L. H. Uppadine and J.-M. Lehn, Grid-type Metal Ion Architectures: Functional Metallosupramolecular Arrays, *Angew. Chem. Int. Ed.*, **43**, (2004), 3644-3662.
6. S. J. van der Molen, P. Liljeroth, Charge Transport through Molecular Switches, *J. Phys.: Condens. Matter*., **22**, (2010), 133001 (1-30).
7. O. Kahn, *Molecular Magnetism*, Eds.; Wiley-VCH.: New York, August **1993**.
8. P. Gütlich, Y. Garcia and H. A. Goodwin, Spin Crossover Phenomena in Fe(II) Complexes, *Chem. Soc. Rev*., **29**, (2000), 419-427.
9. P. Gütlich and A. Hauser, Thermal and Light-induced Spin Crossover in Iron(II) Complexes, *Coord. Chem. Rev*., **97**, **(**1990), 1-22.
10. A. Hauser, Reversibility of Light-induced Excited Spin State Trapping in the $Fe(Ptz)_6(BF_4)_2$ and the $Zn_{1-x}Fe_x(Ptz)_6(BF_4)_2$ Spin-crossover Systems, *Chem. Phys. Lett*., **124**, (1986), 543-548.
11. M. Marchivie, P. Guionneau, J. A. K. Howard, G. Chastanet, J-F. Létard, A. E. Goeta and D. Chasseau, Structural Characterization of a Photoinduced Molecular Switch, *J. Am. Chem. Soc*., **124**, (2002), 194-195.
12. K. Kato, M. Takata, Y. Moritomo, A. Nakamoto and N. Kojima, On-off Optical Switching of the Magnetic and Structural Properties in a Spin-crossover Complex. *Appl. Phys. Lett*., **90**, (2007), 201902 (1-3).
13. A. Bousseksou, G. Molnár, J.-P. Tuchagues, N. Menéndez, É. Codjovi and F. Varret, Triggering the Spin-crossover of $Fe(Phen)_2(NCS)_2$ by a Pressure Pulse: Pressure and Magnetic Field Induced 'Mirror Effects', *C. R. Chimie*., **6**, (2003), 329-335.
14. N. Baadji, M. Piacenza, T. Tugsuz, F. Della Sala, G. Maruccio and S. Sanvito, Electrostatic Spin Crossover Effect in Polar Magnetic Molecules, *Nature Mater*., **8**, (2009), 813-817.
15. V. Meded, A. Bagrets, K. Fink, R. Chandrasekar, M. Ruben, F. Evers, A. Bernand-Mantel, J. S. Seldenthuis, A. Beukman and H. S. J. van der Zant, Electrical Control over the Fe(II) Spin Crossover in a Single Molecule: Theory and Experiment, *Phys. Rev. B*, **83**, (2011), 245415 (1-13).

16. E. J. Devid, P. N. Martinho, M. V. Kamalakar, Ú. Prendergast, C. Kübel, T. Lemma, J.-F. Dayen, T. E. Keyes, B. Doudin, M. Ruben and S. J. van der Molen, The Influence of Molecular Mobility on the Properties of Networks of Gold Nanoparticles and Organic Ligands, *Beilstein J. Nanotechnol.*, **5**, (2014), 1664-1674.
17. M. Cavallini, I. Bergenti, S. Milita, J. C. Kengne, D. Gentili, G. Ruani, I. Šalitroš, V. Meded and M. Ruben, Thin Deposits and Patterning of Room-Temperature-Switchable One-dimensional Spin-crossover Compounds, *Langmuir*, **27**, (2011), 4076-4081.
18. Z. Arcis-Castíllo, S. Zheng, M. A. Siegler, O. Roubeau, S. Bedoui and S. Bonnet, Tuning the Transition Temperature and Cooperativity of Bapbpy-based Mononuclear Spin-crossover Compounds: Interplay between Molecular- and Crystal Engineering, *Chem. Eur. J.*, **17**, (2011), 14826-14836.
19. R. Chandrasekar, F. Schramm, O. Fuhr and M. Ruben, An Iron(II) Spin-transition Compound with Thiol Anchoring Groups, *Eur. J. Inorg. Chem.*, **17**, (2008), 2649-2653.
20. I. Šalitroš**,** O. Fuhr, A. Eichhöfer, R. Kruk, J. Pavlik, L. Dlháň, R. Boča and M. Ruben, The Interplay of Iron(II) Spin Transition and Polymorphism, *Dalton Trans*., **41**, (2012), 5163-5171.
21. T. G. Gopakumar, F. Matino, H. Naggert, A. Bannwarth, F. Tuczek and R. Berndt, Electron-induced Spin Crossover of Single Molecules in a Bilayer on Gold, *Angew. Chem., Int. Ed.*, **51**, (2012), 6262-6266.
22. T. Miyamachi, M. Gruber, V. Davesne, M. Bowen, S. Boukari, L. Joly, F. Scheurer, G. Rogez, T. K. Yamada, P. Ohresser, E. Beaurepaire and W. Wulfhekel, Robust Spin Crossover and Memristance Across a Single Molecule, *Nat. Commun*., **3**, (2012), 1-6.
23. A. Pronschinske, R. C. Bruce, G. Lewis, Y. Chen, A. Calzolari, M. Buongiorno-Nardelli, D. A. Shultz, W. You and D. B. Dougherty, Iron(II) Spin Crossover Films on Au(111): Scanning Probe Microscopy and Photoelectron Spectroscopy, *Chem. Commun.*, **49**, (2013), 10446-10452.
24. M. Bernien, D. Wiedemann, C. F. Hermanns, A. Krüger, D. Rolf, W. Kroener, P. Müller, A. Grohmann and W. Kuch, Spin Crossover in a Vacuum-deposited Submonolayer of a Molecular Iron(II) Complex, *J. Phys. Chem. Lett.*, **3**, (2012), 3431-3434.
25. X. Zhang, T. Palamarciuc, J.-F. Létard, P. Rosa, E. V. Lozada, F. Torres, L. G. Rosa, B. Doudin and P. A. Dowben, The Spin State of a Molecular Adsorbate Driven by the Ferroelectric Substrate Polarization, *Chem. Commun.*, **50**, (2014), 2255-2257.
26. I. Suleimanov, J. S. Costa, G. Molnár, L. Salmon and A. Bousseksou, The Photo-thermal Plasmonic Effect in Spin Crossover@Silica-Gold Nanocomposites, *Chem. Commun*., **50**, (2014), 13015-13018.
27. B. Warner, J. C. Oberg, T. G. Gill, F. El Hallak, C. F. Hirjibehedin, M. Serri, S. Heutz, M.-A. Arrio, P. Sainctavit, M. Mannini, G. Poneti, R. Sessoli and P. Rosa, Temperature- and Light-induced Spin Crossover Observed by X-ray Spectroscopy on Isolated Fe(II) Complexes on Gold, *J. Phys. Chem. Lett.*, **4**, (2013), 1546-1552.
28. R. P. Andres, J. D. Bielefeld, J. I. Henderson, D. B. Janes, V. R. Kolagunta, C. P. Kubiak, W. J. Mahoney and R. G. Osifchin, Self-assembly of a Two-dimensional

Superlattice of Molecularly Linked Metal Clusters, *Science*, **273**, (1996), 1690-1693.
29. T. B. Tran, I. S. Beloborodov, X. M. Lin, T. P. Bigioni, V. M. Vinokur and H. M. Jaeger, Multiple Cotunneling in Large Quantum Dot Arrays, *Phys. Rev. Lett.*, **95**, (2005), 076806 (1-4).
30. J. Liao, L. Bernard, M. Langer, C. Schönenberger and M. Calame, Reversible Formation of Molecular Junctions in 2D Nanoparticle Arrays, *Adv. Mat.*, **18**, (2006), 2444-2447.
31. L. Bernard, Y. Kamdzhilov, M. Calame, S. J. van der Molen, J. Liao and C. Schönenberger, Spectroscopy of Molecular Junction Networks Obtained by Place Exchange in 2D Nanoparticle Arrays**,** *J. Phys. Chem. C.*, **111**, (2007), 18445-18450.
32. J. W. Slot and H. J. Geuze, A New Method of Preparing Gold Probes for Multiple Labeling Cytochemistry, *Eur. J. Cell Biol.*, **38**, (1985), 87-93.
33. J.-F. Dayen, V. Faramarzi, M. Pauly, N. T. Kemp, M. Barbero, B. P. Pichon, H. Majjad, S. Begin-Colin and B. Doudin, Nanotrench for Nano and Microparticle Electrical Interconnects, *Nanotechnology*, **21**, (2010), 335303 (1-7).
34. J.-F. Dayen, E. Devid, M. V. Kamalakar, D. Golubev, C. M. Guédon, V. Faramarzi, B. Doudin and S. J. van der Molen, Enhancing the Molecular Signature in Molecule-nanoparticle Networks via Inelastic Cotunneling, *Adv. Mat.*, **25**, (2013), 400-404.
35. K. B. Biggs, J. P. Camden, J. N. Anker and R. P. van Duyne, Surface-enhanced Raman Spectroscopy of Benzenethiol Adsorbed from the Gas Phase onto Silver Film over Nanosphere Surfaces: Determination of the Sticking Probability and Detection Limit Time, *J. Phys. Chem. A*, **113**, (2009), 4581-4586.
36. J. Larionova, L. Salmon, Y. Guari, A. Tokarev, K. Molvinger, G. Molnár and A. Bousseksou, Towards the Ultimate Size Limit of the Memory Effect in Spin-crossover Solids, *Angew. Chem. Int. Ed.*, **47**, (2008), 8236-8240.
37. E. Coronado, J. R. Galán-Mascarós, M. Monrabal-Capilla, J. García-Martínez and P. Pardo-Ibáñez, Bistable Spin-crossover Nanoparticles Showing Magnetic Thermal Hysteresis near Room Temperature, *Adv. Mat.*, **19**, (2007), 1359-1361.
38. T. B. Tran, I. S. Beloborodov, J. Hu, X. M. Lin, T. F. Rosenbaum and H. M. Jaeger, Sequential Tunneling and Inelastic Cotunneling in Nanoparticle Arrays, *Phys. Rev. B*, **78**, (2008), 075437(1-9).
39. M. Pauly, J.-F. Dayen, D. Golubev, J.-B. Beaufrand, B. P. Pichon, B. Doudin and S. Bégin-Colin, Co-tunneling Enhancement of the Electrical Response of Nanoparticle Networks, *Small*, **8**, (2012), 108-115.
40. J. Liao, S. Blok, S. J. van der Molen, S. Diefenbach, A. W. Holleitner, C. Schönenberger, A. Vladyka and M. Calame, Ordered Nanoparticle Arrays Interconnected by Molecular Linkers: Electronic and Optoelectronic Properties, *Chem. Soc. Rev.*, **44**, (2014), 999-1014.
41. Y. Wang, C. Guan, J. Sun, L. Peng and J. Liao, Transition of Temperature Coefficient of Conductance in Weakly Coupled Gold Nanoparticle Arrays, *Appl. Phys. Lett.*, **105**, (2014), 233116 (1-5).

42. N. Baadji and S. Sanvito, Giant Resistance Change Across the Phase Transition in Spin-crossover Molecules, *Phys. Rev. Lett.*, **108**, (2012), 217201(1-5).
43. F. Evers, F. Weigend and M. Köntopp, Conductance of Molecular Wires and Transport Calculations Based on Density-functional Theory, *Phys. Rev. B*, **69**, (2004), 235411(1-9).
44. A. Arnold, F. Weigend and F. Evers, Quantum Chemistry Calculations for Molecules Coupled to Reservoirs: Formalism, Implementation, and Application to Benzenedithiol, *J. Chem. Phys.*, **126**, (2007), 174101(1-14).
45. R. Ahlrichs, M. Bär, M. Häser, H. Horn and C. Kölmel, Electronic Structure Calculations on Workstation Computers: The Program System Turbomole, *Chem. Phys. Lett.*, **162**, (1989), 165-169.
46. A. Schäfer, H. Horn and R. Ahlrichs, Fully Optimized Contracted Gaussian Basis Sets for Atoms Li to Kr, *J. Chem. Phys.*, **97**, (1992), 2571-2577.
47. A. Schäfer, C. Huber and R. Ahlrichs, Fully Optimized Contracted Gaussian Basis Sets of Triple Zeta Valence Quality for Atoms Li to Kr, *J. Chem. Phys.*, **100**, (1994), 5829-5835.
48. M. Ruben, A. Landa, E. Lörtscher, H. Riel, M. Mayor, H. Görls, H. B. Weber, A. Arnold, and F. Evers, Charge Transport Through a Cardan-joint Molecule, *Small*, **4**, (2008), 2229-2235.
49. J. P. Perdew, Density-functional Approximation For the Correlation Energy of the Inhomogeneous Electron Gas, *Phys. Rev. B*, **33**, (1986), 8822-8824.
50. A. D. Becke, Density-functional Exchange-energy Approximation with Correct Asymptotic Behavior, *Phys. Rev. A*, **38**, (1988), 3098-3100.
51. C. Lee, W. Yang and R. G. Parr, Development of the Colle-Salvetti Correlation-energy Formula into a Functional of the Electron Density, *Phys. Rev. B*, **37**, (1988), 785-789.
52. A. D. Becke, Density-functional Thermochemistry. III. The Role of Exact Exchange, *J. Chem. Phys.*, **98**, **(**1993), 5648-5652.
53. J. M. Holland, J. A. McAllister, C. A. Kilner, M. Thornton-Pett, A. J. Bridgeman and M. A. Halcrow, Stereochemical Effects on the Spin-state Transition Shown by Salts of $[FeL_2]^{2+}$ [L = 2,6-di(Pyrazol-1-yl)Pyridine], *J. Chem. Soc. Dalton Trans.*, (2002), 548-554.
54. P. S. Braterman, J.-I. Song and R. D. Peacock, Electronic Absorption Spectra of The Iron(II) Complexes of 2,2'-bipyridine, 2,2'-bipyrimidine, 1,10-phenanthroline, and 2,2':6',2''-terpyridine and Their Reduction Products, *Inorg. Chem.*, **31**, (1992), 555-559.
55. M. Gerloch and E. C. Constable, Eds., *Transition Metal Chemistry*: *The Valence Shell in d-Block Chemistry; VCH*.: Weinheim, June **1994**.
56. I. Šalitroš, J. Pavlik, R. Boča, O. Fuhr, C. Rajadurai and M. Ruben, Supramolecular Lattice-solvent Control of Iron(II) Spin Transition Parameters, *CrystEngComm.*, **12**, (2010), 2361-2368.
57. S. Kirkpatrick, Percolation and Conduction, *Rev. Mod. Phys.*, **45**, (1973), 574-588.
58. D. S. McLachlan, M. Blaszkiewicz and R. E. Newnham, Electrical Resistivity of Composites, *J. Am. Ceram. Soc.*, **73**, (1990), 2187-2203.
59. J. Wu and D. S. McLachlan, Percolation Exponents and Thresholds Obtained From The Nearly Ideal Continuum Percolation System Graphite-boron Nitride, *Phys. Rev. B*, **56**, (1997), 1236-1248.

60. N. I. Lebovka, S. Tarafdar and N. V. Vygornitskii, Computer Simulation of Electrical Conductivity of Colloidal Dispersions during Aggregation, *Phys. Rev. E.*, **73**, (2006), 031402 (1-6).
61. J. C. Wierman, Bond Percolation on Honeycomb and Triangular Lattices, *Adv. Appl. Probab.*, **13**, (1981), 298-313.